HHS Public Access

Author manuscript

Dev Cell. Author manuscript; available in PMC 2024 August 21.

Published in final edited form as:

Dev Cell. 2023 August 21; 58(16): 1477–1488.e5. doi:10.1016/j.devcel.2023.05.019.

Loss of TJP1 disrupts gastrulation patterning and increases differentiation toward the germ cell lineage in human pluripotent stem cells

Ivana Vasic[1,2,9], **Ashley RG Libby**[1,3,#a], **Annie Maslan**[2,4,5], **Emily A Bulger**[1,3], **David Zalazar**[1,#b], **Martina Z Krakora Compagno**[1,#c], **Aaron Streets**[2,4,5,6], **Kiichiro Tomoda**[1,7], **Shinya Yamanaka**[1,7,*], **Todd C McDevitt**[1,8,#d,*]

[1]Gladstone Institute of Cardiovascular Disease, Gladstone Institutes, San Francisco, CA, USA 94158

[2]UC Berkeley-UC San Francisco Graduate Program in Bioengineering, University of California, San Francisco, San Francisco, CA, USA 94158

[3]Developmental and Stem Cell Biology Ph.D. Program, University of California, San Francisco, San Francisco, CA, USA 94158

[4]Department of Bioengineering, University of California, Berkeley, CA, USA 94720

[5]Center for Computational Biology, University of California, Berkeley, CA, USA 94720

[6]Chan Zuckerberg Biohub, San Francisco, CA, USA 94158

[7]Center for iPS Cell Research and Application, Kyoto, Japan 606-8397

[8]Department of Bioengineering and Therapeutic Sciences, University of California, San Francisco, CA, USA 94158

SUMMARY

[*]Correspondence: Shinya Yamanaka (shinya.yamanaka@gladstone.ucsf.edu) and Todd McDevitt (todd.mcdevitt@gladstone.ucsf.edu).
[9]Lead Contact: Ivana Vasic (ivana.vasic@gladstone.ucsf.edu).
[#a]Current address: The Francis Crick Institute, London, UK 1AT
[#b]Current address: Department of Biomedical Engineering, University of California, Irvine, CA, USA 92697
[#c]Current address: Department of Molecular Biophysics, Florida State University, Tallahassee, FL, USA 32306
[#d]Current address: Sana Biotechnology, South San Francisco, CA, USA 94080

AUTHOR CONTRIBUTIONS

Conceptualization, I.V., A.R.G.L., S.Y., K.T., T.C.M.; Methodology, I.V.; Software, I.V., A.M., and M.Z.K.C.; Validation, I.V., D.Z., and M.Z.K.C.; Formal Analysis and Data Curation I.V. and A.M.; Investigation, I.V. and D.Z.; Resources, A.M., E.A.B., and A.S.; Writing-Original Draft, I.V.; Writing-Review and Editing, I.V., A.R.G.L., A.M., E.A.B., K.T., S.Y., T.C.M.; Visualization, I.V.; Supervision, A.S., K.T., S.Y., T.C.M.; Funding Acquisition S.Y. and T.C.M.

DECLARATION OF INTERESTS

I.V. is the founder and chief executive officer of Vitra Labs, Inc. K.T. is on the scientific advisory board of I Peace, Inc., without salary. S.Y. is a scientific advisor to iPS Academia Japan, Orizuru Therapeutics, and Altos Labs without salary. T.C.M. is Vice President of Cell Engineering at SanaX. I.V. and T.C.M.. are inventors on a patent filing by the Gladstone Institutes and the University of California, San Francisco relating to high-throughput generation of primordial germ cell like cells (PGCLCs).

Biological patterning events that occur early in development establish proper tissue morphogenesis. Identifying the mechanisms which guide these patterning events is necessary for understanding the molecular drivers of development and disease, and to build tissues *in vitro*. In this study, we use an *in vitro* model of gastrulation to study the role of tight junctions and apical/basolateral polarity in modulating bone morphogenic protein-4 (BMP4) signaling and gastrulation-associated patterning in colonies of human pluripotent stem cells (hPSCs). Disrupting tight junctions via knockdown (KD) of the scaffolding tight junction protein-1 (TJP1, also known as ZO1) allows BMP4 to robustly and ubiquitously activate pSMAD1/5 signaling over time, resulting in loss of the patterning phenotype and marked differentiation bias of pluripotent stem cells to primordial germ cell-like cells (PGCLCs). These findings give important insights into how signaling events are regulated and lead to spatial emergence of diverse cell types *in vitro*.

eTOC Blurb

In this study, Vasic et al. examine how tight junction integrity affects receptivity to signaling proteins and patterning in an hPSC model of gastrulation. They demonstrate that knockdown of TJP1, a core tight junction component, in hPSCs results in sustained pSMAD1/5 activity and bias towards PGCLC specification upon treatment with BMP4.

Graphical Abstract

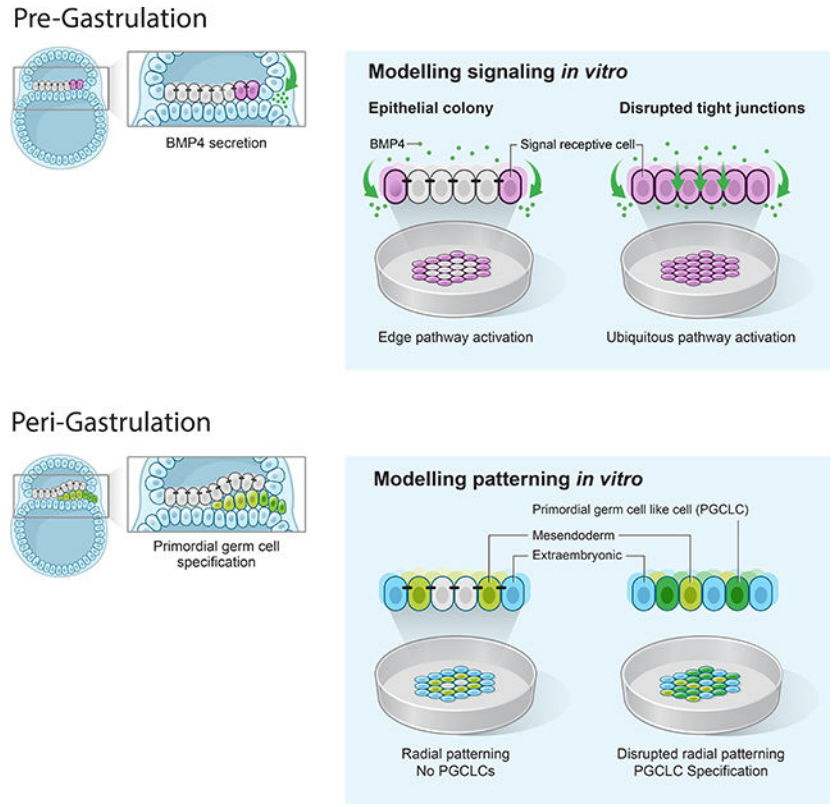

INTRODUCTION

Early in embryonic development, gradients of signaling molecules guide the spatial organization and specification of stem cells to generate a blueprint for axis formation and subsequent tissue growth[1–3]. One of the earliest biological patterning events occurs in the epiblast, when pluripotent cells differentiate and segregate into the three somatic germ layers (endoderm, mesoderm, and ectoderm), in a process known as gastrulation. Understanding how signaling gradients first emerge, take shape, and are interpreted by cells during gastrulation is important for understanding the fundamental principles which guide patterning and morphogenesis of tissues.

Prior to gastrulation, the epiblast is an epithelial tissue reinforced by tight junction complexes. These complexes are comprised of an intracellular scaffold, which partitions the phospholipid bilayer into apical and basolateral domains, and a set of transmembrane proteins, which prevent paracellular diffusion of macromolecules between the apical-facing and basolateral-facing lumens[4–6]. Many signaling protein/receptor families responsible for regulating the gastrulation program such as BMP4, WNT3, and NODAL have conserved basolateral sorting motifs or are reported to be secreted basolaterally[7–11], whereas NOGGIN is secreted apically[12]. This ligand/receptor orientation implicates epithelial structure and cell polarity as critical determinants of morphogen gradient shape and subsequent cell type patterning during gastrulation via asymmetric attenuation of cellular response to morphogen signaling[9,13]. In addition to spatial patterning imposed by epithelial structure, previous studies have proposed that morphogens can autonomously form patterns that lead to germ layer segregation during gastrulation, as described by Alan Turing’s reaction diffusion (RD) and Lewis Wolpert’s positional information (PI) models[14–20]. However, a lack of mechanistic insight hinders our understanding of the possible interplay between tight junction expression and RD/PI in the context of gastrulation patterning.

Seminal work shows that gastrulation-associated patterning events, including the emergence of ectoderm-like, mesendoderm-like, and extraembryonic-like cells in a radial pattern, can be recapitulated in culture by confining hPSCs to circular micropatterns and stimulating with BMP4[21,22]. BMP4, which acts through phosphorylation of the signal transducer SMAD1, is known to be an important initial cue in the gastrulation cascade[23,24]. Follow-up studies suggest that patterning in this system follows an RD/PI process, as BMP4 driven phosphorylation of SMAD1 and subsequent pathway activation causes cells in the colony to secrete both BMP4 and its inhibitor NOGGIN in a feedback loop[20]. Differences in the diffusivities between NOGGIN and BMP4 are thought to create a steady-state gradient of effective BMP4 concentrations across the colony, and cells are presumed to sense positional information and differentiate based both on this concentration gradient and its overlap with other members of the BMP4-induced feedback loop, including WNT3 and NODAL[19,20].

Contradictory reports confound our understanding of the extent to which tight junctions influence ligand-receptor accessibility, signaling pathway activation, and subsequent RD/PI driven germ layer patterning in this system. For example, Etoc et al. demonstrate that changes in apical/basolateral polarity occur on the edge of micropatterned colonies, presumably due to regional loss of tight junctions. They propose that these polarity

changes lead to differential receptor accessibility and preferential pathway activation on the colony edge, and that this edge activation is necessary for radial patterning[19]. However, disruption of tight junction assembly throughout hPSC colonies via calcium chelation does not result in disruption of the radial patterning phenotype. Calcium chelation in addition to ROCK inhibition does disrupt patterning[19]; however, these macroscale and non-specific perturbations make it difficult to decipher whether and how tight junctions are involved in signaling and patterning. Alternatively, Tewary et al. show that pathway activation is ubiquitous throughout micropatterned colonies at earlier timepoints. These results challenge the role of differential receptor accessibility caused by tight junction expression and implicate secreted inhibitors as the primary regulators of patterning[20].

In this study, we use a modified *in vitro* hPSC gastrulation model which maintains epithelial structure over time and recapitulates the characteristics of the epiblast prior to gastrulation. We target tight junctions specifically by knocking down TJP1, a critical component of the tight junction complex[25,26], to study the effects of tight junction expression on signaling pathway activation, gastrulation-associated patterning, and cell specification. We demonstrate that TJP1 KD increases cellular receptiveness to BMP4 and causes ubiquitous and sustained signaling pathway activation, which appears to override endogenous NOGGIN inhibitor activity throughout the colony. Significant changes in multicellular patterning and proportions of different cell types in the TJP1 KD (TKD) versus control hPSC (TWT) colonies establish TJP1 as a key regulator of patterning in our gastrulation model. Additional characterization of cell type emergence demonstrates that TKD colonies differentiate robustly towards PGCLC fates. By comparing the ground state of TWT and TKD cells, we show that PGCLC fate bias is predominantly a result of heightened and sustained BMP4 signaling pathway activation that can be recapitulated in TWT cells. These results provide key insights both into how tight junction complexes within the embryo may shape signaling and morphological patterning, and the importance of epithelial structure in influencing hPSC differentiation *in vitro*.

RESULTS

BMP Pathway Activation Correlates with Regional Loss of TJP1

hPSCs confined to circular micropatterns and treated for 42–48 hours with BMP4 undergo radial patterning of gastrulation-associated markers CDX2 (extraembryonic-like), TBXT (mesendoderm-like), and SOX2 (ectoderm-like)[21,22]. Our lab and others have demonstrated that similarly-sized colonies whose growth is not confined by micropatterns undergo analogous radial patterning in response to BMP4 stimulation[27,28,29] (Figure 1A). In this modified protocol, ~50–100 hPSCs are aggregated overnight within pyramidal microwells, and the following day these 3D aggregates are re-plated sparsely and allowed to grow into distinct 2D colonies that reach 300–500μm in diameter. Compared with micropatterned colonies, unconfined colonies maintained a relatively uniform cell density and a robust epithelial morphology over time (Figure S1A, S1B, S1C). This is critical given that epithelial integrity is a direct function of cell density, and previous reports have linked changes in signaling and cell specification with regional changes in cell density[19,30,31,32]. Our unconfined colonies recapitulate the same aspects of gastrulation patterning as the

micropatterned models (radial germ layer segregation, distinct boundary formation, etc.), but are unique in that they maintain the epithelial structural characteristics of the epiblast prior to and during gastrulation.

Others have demonstrated that low cell densities prevent proper tight junction formation and presumably enhance permeability to signaling proteins[19]. Interestingly, we found the opposite is also true: in monolayer culture at high cell densities, the honeycomb-like intercellular protein expression pattern of TJP1, which is indicative of an intact epithelium, became disrupted and punctate (Figure S1D). High magnification confocal imaging identified that in highly dense regions with punctate TJP1, cells grew on top of each other instead of in a monolayer, forming pseudo-3D structures with aberrant tight junction formation (Figure S1E). Moreover, regions with punctate TJP1 expression, which increase in frequency as cell density increases, overlapped with regions of BMP4-induced signaling pathway activation (phosphorylation of SMAD1/5) (Figure S1D). Therefore, both very low and very high cell densities can cause increases in epithelial permeability. In our experience, punctate TJP1 expression is also present in micropatterned colonies; regions of high density lose TJP1 and overlap with pSMAD1/5 activation upon BMP4 stimulation (Figure S1A). Discrepancies in previously reported pSMAD1/5 pre-patterns may therefore be partially attributed to regional changes in cell density that perturb epithelial structure.

TJP1 expression is inversely correlated with pSMAD1/5 activation even in the context of unconfined colonies with uniform density. For example, upon induction with BMP4, pSMAD1/5 activity was primarily limited to the cells on the edge at earlier timepoints (15 min – 1 hour) (Figure 1B, S1A, 2E). We and others noticed that TJP1 expression does not fully extend to the edge of the colony, and tapers off a distance of approximately one cell layer before reaching the edge[33]. Co-staining of TJP1 and pSMAD1/5 in unconfined colonies after 1 hour of BMP4 stimulation showed an anti-correlation between pSMAD1/5 positive and TJP1 positive regions (Figure 1B). We used CellProfiler[34] (see STAR Methods) to visualize and quantify pSMAD1/5 and TJP1 fluorescence signal at different radial distances from the colony center and normalized these values to LMNB1 nuclear signal, demonstrating the inverse relationship between pSMAD1/5 and TJP1 (Figure 1C, 1D). Given that initial pSMAD1/5 pre-patterning has been implicated in regulating subsequent gastrulation-associated patterning in micropatterned colonies[19,20], we aimed to elucidate the effect of tight junctions on pluripotent morphogenic signaling and gastrulation patterning.

TJP1 Knockdown Leads to Ubiquitous and Sustained Pathway Activation

In vitro, hPSCs are cultured as epithelial sheets that have tight junctions and display apical/basolateral polarity[35], with most morphogen receptors, including BMP receptors BMPR1A, BMPR2, and ACVR2A, localized to the basolateral side[9,19]. These receptors are physically partitioned away from morphogens present in the soluble media on the apical side. As a result, tight junction expression presumably attenuates cellular response to exogenous morphogen signals *in vitro* (Figure 2A).

In order to examine how tight junctions affect cellular receptiveness to signaling in unconfined colonies and, in turn, pattern formation, we sought to knockdown a tight junction component in hPSCs using a DOX-inducible CRISPR interference (CRISPRi) system[36]

(Figure S2A). We targeted TJP1 because it forms dual purpose adhesion plaques that are critical both for maintaining apical/basolateral polarity and barrier function. We created both male (WTC) and female (WTB) hPSC TJP1 KD lines. The WTC line also contains a LMNB1-GFP fusion reporter for live nuclear visualization. TJP1 RNA and protein expression are significantly depleted after five days of DOX treatment, as shown by qPCR, RNA sequencing, immunofluorescence (IF), and western blot (Figures 2B, S2B, 2C, S2C), and both the WTC and WTB TJP1 CRISPRi lines are karyotypically normal (Figure S2D). We performed most of the characterization in the WTC TJP1 CRISPRi line either without or with a minimum of 5 days of DOX treatment (referred to in the text as TWT and TKD, respectively); however, several supplemental figures show phenotype reproducibility in the WTB TJP1 CRISPRi line.

Prior to BMP4 exposure, we observed distinct morphology between TWT and TKD cells in standard culture. TKD cells grew in denser colonies and exhibited changes in nuclear shape (Figure S2E, S2F). Where TWT nuclei were stretched and flat, TKD nuclei were taller and rounder. When grown as unconfined colonies and exposed to BMP4, TWT cells largely limited pSMAD1/5 expression to the colony edge at early timepoints (15 min – 1 hour). At later timepoints (6 hours), pSMAD1/5 was detectable in cells located centrally within the colony; however, due to well-known inhibitor feedback loops[19,20], this pathway activation was shut off by 48 hours (Figure 2D, 2E). Strikingly, at early timepoints, the TKD colonies displayed pSMAD1/5 throughout the colony. Furthermore, TKD cells maintained pSMAD1/5 activation over time, despite significant increases in transcription and secretion of the secreted BMP inhibitor NOGGIN (Figure S3A, S3B), which is implicated in SMAD1/5 inactivation in TWT cells over time[20]. In TWT cells, NOGGIN is secreted apically and is trafficked transepithelially with assistance from glycoproteins on the apical surface[12]. The maintenance of pSMAD1/5 pathway activation despite increased NOGGIN expression and secretion in TKD colonies suggests that TJP1 is not only important for preventing ligands such as BMP4 from accessing basolateral receptors, but may also be necessary to render the cells sensitive to some inhibitors; either by maintenance of apical surface glycoproteins or sequestration and concentration of other basolaterally secreted morphogen inhibitors within the colony interior.

Signaling Changes Are a Result of Increased Permeability in TKD Cells

In order to confirm basolateral sequestration of BMP receptors within an epithelium, hPSCs were grown on a transwell membrane, where apical and basolateral sides of the media are independently accessible. As expected, basolateral presentation of BMP4 was required for pSMAD1/5 activation in TWT cultures (Figure S3C). Alternatively, both apical and basolateral stimulation activated pSMAD1/5 in TKD cells (Figure S3C). Given that BMP receptor gene expression does not considerably differ between TWT and TKD cells (Figure S3D), two main possibilities could explain this phenomenon. The first is that loss of TJP1 causes mixing of apical/basolateral domain elements through the plasma membrane and disrupts trafficking of receptors to their proper domains (loss of apical/basolateral polarity). The second is that loss of TJP1 causes increased permeability to signaling molecules (loss of barrier function). To test these possibilities, we first looked to characterize apical/basolateral polarity between TWT and TKD cells.

In polarized cells, the Golgi apparatus faces the apical side (secretory domain)[37,38]; therefore, we examined the positioning of the Golgi in TWT and TKD cells. To agnostically visualize the cells' apical facing surface, we used the F-Actin stain phalloidin. Confocal z-stacks of cell colonies stained for both F-Actin and Golgin97 identified that in both cell types, the Golgi sits on top of the nucleus facing the apical side of the cell (Figure S3E). Quantification of the distance between the apical surface and the nucleus/Golgi confirmed that on average, the Golgi is closer to the apical surface than the nucleus is in both TWT and TKD cells (Figure S3F). Next, to characterize membrane polarity and potential changes in receptor accessibility, we stained TWT and TKD colonies for well-known apical polarity proteins, Ezrin and PKC$_\zeta$, and basolateral BMP receptor BMPR1A. In all colonies imaged, apical proteins could be found on the apical surface of the cells, distinctly separated from BMPR1A which presented basolaterally, even in TKD cells (Figures S3E, S3F). Our findings are consistent with other studies performed in epithelial Madin-Darby Canine Kidney (MDCK) cells, which demonstrate that knockdown of TJP1 does not cause changes in polarization of apical and basolateral membrane elements in 2D[39–43].

Next, we performed a FITC-based diffusion assay to look for differences in permeability of TWT and TKD hPSC monolayers. To do this, we grew each cell type on a transwell membrane and added 40kDa dextran conjugated with FITC to the apical compartment (Figure 2F). 40kDa-FITC was selected due to its similarity in size and hydraulic radius to BMP4. Fluorescence measurements of the basolateral compartment over time allowed us to quantify permeability of the TKD compared to TWT cells. We found that significant increases in FITC diffusion through TKD cell layers could be observed as early as 30 minutes following treatment (Figure 2F). Similarly, transepithelial resistance (TEER) measurements performed on TWT and TKD monolayers confirmed that TKD cells were not able to form a continuous epithelium that resists passage of ions through the paracellular space (Figure 2G). Therefore, our results suggest that an increase in molecular permeability permits heightened signaling pathway activation seen in TKD cells.

TKD Causes Changes in Cell Fate Proportions in Unconfined Gastrulation Models

The initial pSMAD1/5 edge pre-pattern is assumed to dictate both the shape of a BMP-NOGGIN RD gradient and the subsequent spatiotemporal pSMAD1/5 and gastrulation-like pattern[19,20]. pSMAD2 activation, which occurs through NODAL signaling, is also known to be important for the patterning phenotype, as pharmacological inhibition of NODAL disrupts the emergence of CDX2+ and TBXT+ cells in micropatterned hPSCs stimulated with BMP4[15]. However, Tewary et al. demonstrate that stimulation of micropatterned hPSC colonies solely with NODAL does not lead to gastrulation-like patterning[20], implicating the BMP-NOGGIN gradient and subsequent spatiotemporal pSMAD1/5 activation as the primary driver of patterning in accordance with PI principles[15].

In TWT colonies, cells on the edge that remain pSMAD1/5 positive throughout BMP4 stimulation eventually acquire CDX2+ extraembryonic-like fates[19–21]. Etoc et al. model the edge region as being simultaneously pSMAD1+ and pSMAD2+, a combination predicted to yield CDX2 fates. Therefore, if the current RD/PI paradigm established by Tewary et al. and Etoc et al. is correct, TKD colonies, which mimic the "edge" phenotype and maintain

ubiquitous and sustained pSMAD1/5 activation throughout the entire colony for 48 hours, would be expected to ubiquitously differentiate to the CDX2 lineage following BMP4 treatment (Figure 3A). Accordingly, our results show that TKD colonies treated with BMP4 have increased CDX2 expression across the colony interior. In addition, these colonies display a stark decrease in central SOX2 expression, and disruption of the TBXT ring pattern (Figure 3B, 3C). These results establish TJP1, and therefore tight junction stability, as a key component of BMP4-induced cell fate and spatial patterning.

RNA Sequencing of BMP4-Treated TKD Colonies Indentifies PGCLC Bias

Unexpectedly, we observed that like CDX2, TBXT expression was substantially increased throughout the center of TKD colonies (Figure 3B). Many progenitor cell types express TBXT; therefore, to better identify this population and quantify changes in TKD-induced lineage bias, we performed RNA sequencing on untreated and BMP4-treated (48 hours) TWT and TKD colonies. We found 1099 differentially expressed genes between BMP4 treated TKD and TWT cells, 722 being upregulated and 377 being downregulated. RNA sequencing confirmed IF staining results: CDX2 and TBXT transcripts were highly expressed, whereas SOX2 transcripts were lowly expressed in TKD cells treated with BMP4, compared with TWT cells (Figure 3D). Analysis of a panel of well-known gastrulation-associated lineage markers in TWT and TKD cells identifies that TKD cells tended to express mesendoderm, PGC, and extraembryonic markers at the expense of ectodermal-like lineages (Figure 3D). Gene ontology (GO) analysis performed on clusters 2 and 3 of the top 150 differentially expressed genes (DEGs) between TWT and TKD showed upregulation of endoderm and sex cell-related pathways in TKD colonies (Figure 3E). Similarly, when comparing DEGs between TWT and TKD, analysis identifies significant increases in NANOS3 (logFC=8.92), SOX17 (logFC=8.25), and WNT3 (logFC=6.56), in TKD: all of which are indicative of the human PGC specification program[44] (top 16 DEGs, including NANOS3 and SOX17, are shown in Figure 3F). Subsequent IF staining for PGC markers BLIMP1, TFAP2C, and SOX17 at 48 hours showed increases in expression of these markers in TKD colonies compared with the TWT controls (Figure 4A, 4B). PGCLC differentiation of TKD cells could also be observed in cells grown under standard monolayer conditions (not aggregated or grown into circular colonies) with 48 hours of BMP4 stimulation (Figure 4C–4D). By 72 hours, clear triple positive expression of BLIMP1/TFAP2C/SOX17 was seen in ~36% of TKD cells (Figure 4E–4F) in monolayer culture, a phenotype that was also confirmed in the female WTB TJP1 KD iPSC line (Fig S4A–D). Together, these results suggest that BMP4 stimulation of hPSCs lacking tight junctions dramatically augments cell receptiveness to signals needed for PGCLC emergence.

Decoupling Signaling and Structural Changes in TKD PGCLCs

Upon the discovery of a nascent PGCLC population within our TKD colonies, we next sought to decouple the effects of structural changes due to tight junction instability and ubiquitous pSMAD1/5 activation that might enable the robust emergence of PGCLCs. We first looked to existing literature to understand the required components enabling PGCLC differentiation *in vitro*. Two seminal papers describe different protocols for generating human PGCLCs[44,45]. In the first protocol (Sasaki et al.), hPSCs are pre-induced into an incipient mesoderm-like (iMeLC) state that renders the cells poised for PGCLC

specification. In the second protocol (Irie et al.), hPSCs are first reset from a primed to a naïve pluripotency state, as primed hPSCs are thought to have lost the developmental potential to generate PGCLCs. Indeed, without iMeLC or naïve pluripotency pre-induction, both protocols fail to efficiently generate PGCLCs (1–2% efficiency). However, in our differentiation, TKD cells do not undergo any form of pre-induction yet are able to produce a robust PGCLC population. Two possibilities potentially explain this PGCLC specification bias: 1) loss of TJP1 causes a change in pluripotent ground state (to a naïve- or iMeLC- like state), or 2) signaling changes caused by loss of TJP1 recapitulate *in vivo* PGC specification, and are sufficient to drive PGCLC differentiation *in vitro*.

We first looked to characterize pluripotency in TWT and TKD cells in the absence of BMP4. RNA sequencing results indicated that aside from TJP1 and ZNF10 (which is part of the CRISPRi machinery), few genes were both significantly and substantially differentially expressed between untreated TWT and TKD cells (Figure S4E) in the pluripotent state, and no significant changes were detected in canonical pluripotency markers (Figure S4F). Whole genome bisulfite sequencing demonstrated that while several DNA regions were differentially methylated, there were no global changes in methylation between TWT and TKD cells (Figure S4G), which would be expected if a resetting process to a more naïve pluripotency state occurred. 17 differentially methylated genes were identified; however, GO analysis also did not identify any significant regulatory or functional relationship between the differentially methylated genes. Together, these data suggest that the transcriptome and methylome were not greatly affected by loss of TJP1 and thus, a potential change in the ground state would not explain the TKD predisposition to adopt PGCLC fates. Although there was no evidence to support a change in ground state in untreated TKD cells, we decided to test the possibility that the cells were passing through an accelerated iMeLC-like state before their differentiation into PGCLCs. To do this, we stained for PGCLC markers BLIMP1 and TFAP2C, and the iMeLC marker T, at various times during the 48 hour differentiation of TKD cells. A double positive BLIMP1+/TFAP2C+ PGCLC population became strongly detectable at 36 hours, which coincided with detection of T (Figure S5A). However, there was no overlap in expression of T and BLIMP1 or TFAP2C at any timepoint, suggesting that the TKD cells do not pass through an intermediate iMeLC state.

We next tested the hypothesis that TKD cells are predisposed to PGCLC fates because, unlike TWT cells which are known to experience NOGGIN-related BMP4-pathway inhibition at later timepoints, TKD cells experience sustained BMP4-pathway activation[20]. To decouple changes in signaling from potential structural changes that result from TJP1 knockdown, we looked to recapitulate the pSMAD1/5 signaling dynamics in hPSCs without TJP1 knockdown. To do this, we grew TWT and TKD cells on a transwell membrane. Bi-directional stimulation of hPSCs with BMP4 resulted in ubiquitous and sustained activation of pSMAD1/5 over the course of 48 hours in both TWT and TKD cells, much like when TKD cells are stimulated in standard culture (Figure 5A, 5B). RNA sequencing of stimulated TWT and TKD cells grown on transwells showed remarkable similarities in marker expression between the two samples, demonstrating that most of the observed changes in cell fate were a direct result of increased signal pathway activation. We found 53 DEGs between BMP4 treated TKD and TWT cells grown on transwells, with 36 being upregulated and 17 being downregulated. Overall, the total number of DEGs between TWT

and TKD samples was significantly higher in standard culture (1099) than in transwell (53) culture, highlighting the magnitude of the expression changes dependent solely on changes in pSMAD1/5 signaling. Of these 53 genes, unbiased clustering and GO analysis demonstrated that TKD cells retained a bias towards mesendodermal lineages (Figure 5C).

Interestingly, neither TWT nor TKD cells grown on transwell membranes and treated for 48 hours with BMP4 (50ng/mL) efficiently differentiated to PGCLC fates, as seen for TKD cells on standard plates. We hypothesized that this could be due to excessive signal pathway activation from bi-directional stimulation on the transwell membrane, or mechanical differences between the two plates, which has previously been shown to affect differentiation[46]. By testing a range of BMP4 concentrations, we discovered robust and ubiquitous PGCLC differentiation of TWT cells did occur on the transwell membranes when BMP4 was supplied bi-directionally at 10ng/mL (Figure 5D, 5E). Taken together, these results indicate that changes in cell identity in the absence of TJP1, and specifically the emergence of a PGCLC population, are largely due to increased susceptibility to BMP4 signaling.

DISCUSSION

In this study, we definitively link epithelial structure, maintained by tight junction proteins, with signaling pathway activation and multicellular patterning. We use a gastrulation-like patterning platform which maintains epithelial structure over time to clarify the role of tight junctions and apical/basolateral polarity in shaping the pSMAD1/5 pre-pattern and in directing germ layer patterning. By stably knocking down TJP1 in our system, we disrupt the function of tight junctions and recapitulate “edge” phenotypes in every cell throughout the colony. We demonstrate that perturbing tight junction function causes ubiquitous pSMAD1/5 activation and loss of the pSMAD1/5 edge asymmetry postulated by Etoc et al. to drive the formation of the RD gradient. TJP1 loss also renders cells insensitive to pSMAD1/5 pathway inactivation via NOGGIN, and as a result, disrupts the patterning of germ layer markers. Aside from repression of NOGGIN, few other studies to date have reported perturbations that lead to such a significant loss of patterning as we observe with TJP1 KD, distinguishing TJP1 as a critical regulator of signaling and patterning.

These findings have interesting implications for the role of epithelial structure in the maintenance and controlled emergence of cell types during embryonic development. In the embryo, the significance of the epiblast’s epithelial structure has remained a mystery; however, epithelialization is a well-known hallmark of early development in amniotes, as the epiblast starts as a non-polar aggregate of cells, passes through a semi-polar rosette stage, and eventually forms a laminar epithelial structure thought to be a requisite for subsequent gastrulation[47]. *In vitro* capture of pluripotent stem cells from each of these stages identifies that these cells are transcriptionally and epigenetically distinct, and are maintained by different signaling milieus[48–51]. While we show that changes in epithelial structure do not influence the pluripotent state, our findings suggest that different classes of signaling proteins might be used in signaling of non-polar versus epithelial tissues.

For example, we observe that both NOGGIN and WNT expression increase in TKD colonies, however, the activity of NOGGIN appears to be negligible, as there is no change in the pSMAD1/5 activation profile over time. However, high induction of TBXT-positive cells implies that WNT activity remains high in the colonies. One explanation for this discrepancy could be that compared to WNT, NOGGIN is a long-range inhibitor[52,53] that is secreted apically and relies on trans-epithelial transport to interact with BMP4 ligands which are secreted basolaterally[12]. Previous findings show that despite basolateral BMP4 stimulation, apical NOGGIN is capable of shutting off pSMAD1/5 activation. It is possible that TKD interferes with shuttling functions, explaining inactivity of NOGGIN in the colonies. By contrast, previous evidence suggests that WNT is a short-range, juxtacrine signaling protein[54]. Increases in density that are correlated with loss of epithelial structure are therefore suitable for prolific WNT signaling, and may account for increases in TBXT fates throughout TKD colonies. In other words, epithelial structure may be necessary for signaling by some types of proteins and may interfere with signaling by others, depending on their size, chemical structure, and mechanism of action.

Additionally, regional loss of tight junctions due to increases in density, embryo geometry, or cell-activated breakdown could be an important mechanism for increasing sensitivity to apical signaling cues in specific locations in the embryo. For example, previous studies in the mouse embryo show that there is a break in tight junction expression between the extraembryonic ectoderm (ExE) and the epiblast[9]. The ExE is responsible for secreting BMP4 signals necessary for both PGC differentiation and gastrulation initiation[24]. In mouse and cynomolgus monkeys, PGCs arise in the proximal epiblast directly adjacent to the ExE[55], bordering the region that is reported to have lower expression of tight junctions and higher pSMAD1/5 activity[9]. Given our finding that loss of TJP1 primes hPSCs for PGCLC fates, it is possible that this specific and unique position in the embryo permits future PGCs to be exposed to higher and more sustained levels of BMP compared with the rest of the embryo proper, thereby promoting their specification.

Understanding how TJP1 affects cells' receptiveness to signaling molecules enables us to "unlock" *in vitro* stem cell differentiation protocols for previously intractable cell types, as we did in generating PGCLCs. Our results show that hPSCs in regular culture are largely unresponsive to BMP4 presented apically in the media, an observation that could apply to other types of morphogens as well. RNA sequencing data identify that hPSCs stimulated for 48 hours with BMP4 are transcriptionally similar to unstimulated cells. Therefore, while many differentiation protocols aim to recapitulate exposure to developmentally relevant morphogens, hPSCs in culture are likely not receiving these signals. For example, genetic studies in mouse null mutants lacking genes for BMP4, SMAD1, and SMAD5 fail to develop PGCs, demonstrating that their specification is dependent on the acute activation of the canonical BMP4-SMAD1/5 pathway[55,56]. Previous protocols to generate PGCLCs have relied on excessively high concentrations of BMP4 that far exceed physiological levels and require a dissociation step, which is perhaps inadvertently used to overcome signaling barriers present in standard culture of hPSCs with an epithelial phenotype. However, we and others have shown that tight junctions re-assemble very quickly after aggregation in hPSCs, after which they would confer the same signaling barriers as standard culture and may result in inconsistencies in differentiation. Using temporary pharmacological inhibition of

TJP1 or culturing cells on transwells prior to differentiation could therefore enable precise, controlled, and multiplexed signaling pathway activation, as well as standardization and optimization of many hPSC differentiation protocols.

Patterning events that drive tissue morphogenesis are coordinated by a series of fundamental and interconnected pathways, which span many modes of cellular communication (e.g. paracrine, juxtacrine, extracellular matrix signaling, mechanical push and pull), and are conserved in the development of different tissue types. Identifying key parameters that drive morphogenesis is important for gaining a mechanistic understanding of how tissues develop and therefore also for engineering tissues *in vitro*. Our findings show that tissue structure is an important factor to consider in understanding how morphogen gradients are shaped *in vivo* and in developing robust and reproducible differentiation protocols *in vitro.*

LIMITATIONS OF THE STUDY

A limitation in this study is that we used bulk assays (RNA-sequencing and bisulfite sequencing) to globally characterize cell states in both the pluripotent and differentiated conditions, leading to a lack of resolution of cellular identity at the single cell level. For researchers looking to use the unconfined gastrulation-like model system to test other potential perturbations, please note that due to some variations in colony shape and size that arise from unconfined culture (as compared with micropatterned colony culture) subtle changes in cell fate proportions may be more difficult to detect and quantify in this system.

STAR METHODS

Resource Availability

Lead contact—Further information and requests for resources and reagents should be directed to and will be fulfilled by the lead contact, Ivana Vasic (ivana.vasic@gladstone.ucsf.edu).

Materials availability—Modified plasmids can be made available upon request.

Data and code availability

- RNA sequencing data have been deposited at GEO, and whole genome bisulfite sequencing data have been deposited at SRA. Accession numbers are listed in the key resources table.
- All original code has been deposited at Zenodo. DOIs are listed in the key resources table.
- Any additional information required to reanalyze the data reported in this paper is available from the lead contact upon request.

Experimental Model and Study Participant Details

Cell Lines—The parental human induced pluripotent stem cell lines used in this study are the WTC-mEGFP-LMNB1-CRISPRi line from the Allen Institute (CVCL_IR32, male, passage 32) obtained from Coriel, and the WTB-CRISPRi-Gen1B line from Dr. Bruce

Conklin's lab and the Gladstone Institutes Stem Cell Core (CVCL_VM35, female, passage 40). TJP1 CRISPRi lines were generated in both WTC and WTB, as detailed in the subsequent Method Details section. All cells were maintained in a humidified incubator at 37 °C with 5% CO_2. For routine culture, cells were grown feeder-free on growth factor reduced Matrigel (Corning) and fed daily with mTESR1 medium (Stem Cell Technologies), without or with doxycycline (DOX): TWT (−DOX) and TKD (+DOX). Cells were passaged every 3–4 days with Accutase, and ROCK inhibitor (10μM; Selleckchem) was added to the media to promote cell survival after passaging. All generated cell lines were karyotyped prior to expansion and confirmed normal by Cell Line Genetics. The cells were also regularly tested for mycoplasma using a MycoAlert Mycoplasma Detection Kit (Lonza).

Method Details

Generation of CRISPRi Lines—TJP1 KD was achieved using a DOX inducible CRISPR interference (CRISPRi) system, which is comprised of two components: a dCas9-KRAB repressor driven by a Tet-on-3G promoter knocked in into the AAVS1 safe harbor locus and expressed only under DOX treatment, and a constitutively expressed guide RNA (gRNA) which targets the transcriptional start site of a gene (Figure S2A), described previously by Mandegar et al.[36]. Briefly, to generate the parental line containing CRISPRi machinery, approximately 2 million WTC or WTB derived cells were nucleofected with the knock-in vector (1μg) along with TALENS targeting the AAVS1 locus (0.5μg for each pair) and cultured in mTESR1 and ROCK inhibitor (10μM). Knock-in selection was performed with Geneticin (Thermo Fisher) over the course of 10 days, and a clonal population was generated through colony picking under the EVOS picking microscope in sterile conditions. To achieve TJP1 KD, we designed gRNAs which bind within 150bp of the transcription start site of TJP1 and cloned them into the pgRNA-CKB vector at the BsmB1 restriction site, following the protocol described in Mandegar et al.[36]. Vectors containing each gRNA sequence were individually nucleofected into the WTC-mEGFP-LMNB1-CRISPRi iPSC and the WTB Gen1B CRISPRi iPSC lines using the Human Stem Cell Nucleofector Kit 1 solution with the Amaxa Nucleofector 2b device (Lonza). Nucleofected cells were subsequently seeded at a density of 8,000 cells/cm^2 and recovered in mTESR1 supplemented with ROCK inhibitor (10μM) for two days. Guide selection was performed with Blasticidin (10μg/mL, ThermoFisher Scientific) for seven days, and clonal populations were generated through colony picking. Knockdown efficiency was evaluated through exposure to DOX for five days, after which mRNA was isolated, and relative levels of TJP1 were assessed through qPCR. Levels of TJP1 were normalized to copy numbers from the same line without CRISPRi induction, and the clonal cell line with the most effective knockdown efficiency was selected. Both WTC and WTB TJP1 CRISPRi lines were made using the same plasmid and TJP1 targeting guide (guide sequence is listed in the key resources table).

Generation of Uniform Unconfined Colonies—To generate unconfined colonies of a defined size, we followed previously published protocols[27,64,65]. Briefly, PSCs were passaged and resuspended in mTESR1 supplemented with ROCK inhibitor (10μM). Cells were seeded into 400μmX400μm pyramidal PDMS inserts at a density of ~50–100cells/insert, and inserts were centrifuged at 200 RCF for 3 minutes. The inserts were then

transferred to the incubator and left to condense into aggregates overnight. The following day, the aggregates were resuspended in mTESR1 using a wide bore p1000 pipet tip, to prevent breaking up the aggregates. The cell aggregates were then transferred to a Matrigel-coated 96 well plate at a concentration of approximately ~10 aggregates/well, and left overnight to attach and form 2D colonies. Colonies were subsequently fed with mTESR1 for 1–2 days, until they reached a size approximately 300–500μm in diameter. Alternatively, unconfined colonies can also be generated by seeding disassociated cells sparsely at a density of 2cells/ mm^2 allowing them to grow until they are approximately 300–500μm in diameter. To achieve the gastrulation-like radial colony differentiation, 2D unconfined colonies were treated with mTESR1 supplemented with BMP4 (200μL/well, 50ng/mL, R&D Systems) for 48 hours.

Transwell Culture of hPSCs—Corning Costar Transwell plates with a 6.5mm diameter and 3μm pore size were used. The apical side of the transwell membranes was coated overnight with Matrigel. Prior to seeding, the Matrigel was removed and the membrane was rinsed with PBS+/+. For monolayer transwell experiments (detailed in Figure 2F, S3C, and 5D), cells suspended in mTESR1 supplemented with ROCK inhibitor (10μM) were seeded onto the transwell membranes at a density of 1,000–1,500cells/mm^2. 24 hours after seeding, cells were fed with fresh mTESR1. 48 hours after seeding, the membranes were imaged on an EVOS fluorescence microscope at 10X to visualize whether the GFP labelled cellular nuclei reached confluence and were completely covering the membrane (we have previously determined that this protocol generates intact epithelia at this timepoint - see results in Figure S1D). Upon verifying confluence, the experiments were performed. To perform the FITC diffusion assay (Figure 2F), FITC conjugated to 40-kDa dextran (Sigma-Aldrich) was added to the apical compartment, and fluorescence measurements were taken over time (0 – 7 hours) from basolateral compartment using a plate reader. To perform the pSMAD1/5 directional activation assay (Figure S3C), membranes were treated either from the apical or basolateral compartments with BMP4 (50ng/mL) for 1 hour. To perform the PGCLC transwell differentiation (Figure 5D), membranes were treated from both the apical and basolateral compartments with BMP4 (various concentrations) for 48 hours. For every monolayer transwell experiment, 200μL media was added to the apical compartment and 1mL media was added to the basolateral compartment.

For colony transwell experiments (detailed in Figure 5A), cell aggregates were resuspended in mTESR1 and seeded onto the prepared transwell membrane at a density of 10 aggregates/membrane. 48 hours after seeding, the membranes were treated both apically and basolaterally with mTESR1 supplemented with BMP4 (200μL apical compartment, 1mL basolateral compartment, 50ng/mL) for 48 hours.

Monolayer PGCLC Differentiation—TWT (−DOX) and TKD (+DOX) cells were suspended in mTESR1 supplemented with ROCK inhibitor (10μM) and seeded into 96 well plates at a density ~100cells/mm^2. 24 hours after seeding, cells were fed with fresh mTESR1. 48 hours after seeding, they were treated with mTESR1 supplemented with BMP4 (50ng/mL). mTESR1 with BMP4 was refreshed daily. At 48 and 72 hours after induction with BMP4, the cells were fixed prior to staining for PGCLC lineage markers.

Immunofluorescence Staining—Live cells were rinsed with PBS 1X, fixed in 4% paraformaldehyde (VWR) for 15 minutes, and subsequently washed 3X with PBS. The fixed cells were permeabilized and blocked in 0.3% Triton X-100 (Sigma Aldrich) and 5% normal donkey serum for 1 hour at room temperature, and then incubated with primary antibodies at 4°C overnight (also in 0.3% Triton, 5% normal donkey serum). The following day, samples were washed 3X with PBS and incubated with secondary antibodies in 0.3% Triton and 1% BSA at room temperature for 2 hours. Secondaries used were conjugated with Alexa 647, Alexa 405, and Alexa 555 (Abcam), at a dilution of 1:400.

Image Analysis (CellProfiler and ImageJ)—Quantification of marker expression at various radial distances from the colony center was done using both CellProfiler and custom ImageJ scripts. For the CellProfiler pipeline (used in Figures 1C and 1D), to create a colony object with which to perform subsequent localization measurements, the nuclear LMNB1 channel was first thresholded, dilated, and holes were removed. The colony object was then sliced radially into 25 bins and LMNB1, pSMAD1, and TJP1 object intensity distributions were then measured across the bins (each has a width of approximately 8μm) using the function MeasureObjectIntensityDistribution. pSMAD1/5 and TJP1 fluorescence intensities were then normalized to LMNB1 signal. The custom CellProfiler pipeline used for these figures and a corresponding sample image set for tutorial purposes can be found at: https://github.com/ivanavasic/image_analysis/tree/main/CellProfiler_IntensityDistribution. For the ImageJ pipeline (used in Figure 3C and 4B), the nuclear LMNB1 channel was first thresholded, dilated, and holes were removed. Stepwise erosion was performed and generated radial slices approximately 20um in diameter. Measurements of fluorescence intensity were taken from each slice for LMNB1, CDX2, TBXT, SOX2, or LMNB1, BLIMP1, SOX17, TFAP2C. Transcription factor fluorescence intensities were then normalized to LMNB1 signal. Code for ImageJ scripts is at: https://github.com/ivanavasic/image_analysis/tree/main/ImageJ_StepwiseErosion. Quantification of nuclei with positive marker expression (Figures 2D, 4D, 4F, S4B, S4D, 5B, 5E) was done using CellProfiler, using two different modified versions of the default pipeline for percent positive marker expression[34]. These two CellProfiler pipelines for pSMAD1/5 quantification (Figure 2D, 5B) and for PGCLC marker quantification (Figures 4D, 4F, S4B, S4D, 5E) along with corresponding sample images for tutorial purposes have been uploaded to: https://github.com/ivanavasic/image_analysis/tree/main/CellProfiler_PercentPositive_pSMAD1 and https://github.com/ivanavasic/image_analysis/tree/main/CellProfiler_PercentTriplePositive_PGCLC respectively.

RNA Sequencing and Data Analysis—For RNA sequencing performed on standard plates (Figures S2B, 3D–F, S4E–F), TWT (−DOX) and TKD (+DOX) cells were seeded sparsely onto standard culture 6-well plates in mTESR1 supplemented with ROCK inhibitor (10μM) and allowed to grow into colonies 300–500μm in size, as described above. Subsequently, cell lysates for the untreated (pluripotent) conditions were taken by rinsing the wells once with PBS, and placing 1.5mL RLT buffer/well for 3 minutes. Lysates were frozen and preserved at −80°C. Simultaneously, mTESR1 supplemented with BMP4 (50ng/mL) was added to the remaining wells (BMP4+) conditions. After 48 hours of BMP4 treatment, cell lysates were taken and stored as described above. RNA extraction was performed

using Qiagen's RNeasy kit, and samples were subsequently sent to Novogene for library preparation and sequencing (Illumina, PE150, 20M paired reads).

For RNA sequencing performed on transwell plates (Figure 5C), TWT (−DOX) and TKD (+DOX) cells were seeded sparsely onto in mTESR1 supplemented with ROCK inhibitor (10μM) and allowed to grow into colonies 300–500μm in size, as described above. Subsequently, cell lysates for the untreated (pluripotent) conditions were taken by passaging cells on the membrane with Accutase, and resuspending them directly into RLT buffer. Simultaneously, mTESR1 supplemented with BMP4 (50ng/mL) was added to both the apical and basolateral compartments of the transwell (BMP4+) conditions, and lysate was taken after 48 hours of treatment. Lysate storage and RNA extraction were the same as described above.

An RNA-seq data analysis pipeline was created using Snakemake (v3.13.3) with python (v3.6.10). Adapters were trimmed using trimmomatic (v0.36) in paired end mode with the following parameters: ILLUMINACLIP:TruSeq3-PE.fa:2:30:10 LEADING:3 TRAILING:3 SLIDINGWINDOW:4:15 MINLEN:36. Quality control was performed using FastQC (v0.11.9) and MultiQC (v1.9). Transcripts were quantified using Salmon (v0.14.2) with parameters --validateMappings -l A with the GRCh38 reference transcriptome (downloaded from http://ftp.ensembl.org/pub/release-104/fasta/homo_sapiens/cdna/Homo_sapiens.GRCh38.cdna.all.fa.gz). Differential expression analysis was performed using the voom function in limma. Differential expression was called based on logFC significantly greater than 1 and adjusted p-value < 0.01.

Whole Genome Bisulfite Sequencing and Data Analysis—TWT (−DOX) and TKD (+DOX) cells were seeded and cultured as described in the RNA sequencing section on standard plates. Only untreated (pluripotent) samples were sent for sequencing. To do this, cells were dissociated using Accutase and resuspended in 200μL PBS + proteinase K, and frozen at −20°C for subsequent DNA extraction. DNA extraction was performed using Qiagen's Blood and Tissue DNA extraction kit. Samples were subsequently sent to CD Genomics for whole genome bisulfite sequencing (Illumina, PE150, 250M paired reads). At CD Genomics, 1 μg of genomic DNA was fragmented by sonication to a mean size of approximately 200–400 bp. Fragmented DNA was end-repaired, 5'-phosphorylated, 3'-dA-tailed and then ligated to methylated adapters. The methylated adapter-ligated DNAs were purified using 0.8× Agencourt AMPure XP magnetic beads and subjected to bisulfite conversion by ZYMO EZ DNA Methylation-Gold Kit (zymo). The converted DNAs were then amplified using 25 μL KAPA HiFi HotStart Uracil+ ReadyMix (2X) and 8-bp index primers with a final concentration of 1 μM each. The constructed WGBS libraries were then analyzed by Agilent 2100 Bioanalyzer and quantified by a Qubit fluorometer with Quant-iT dsDNA HS Assay Kit (Invitrogen), and finally sequenced on Illumina Hiseq X ten sequencer.

A bisulfite sequencing data analysis pipeline was created using Snakemake (v3.13.3) with python (v3.6.10). Quality control was performed using FastQC (v0.11.9) and MultiQC (v1.9). Bisulfite analysis was performed using Bismark (v0.22.3) with bowtie2 (v2.3.4.1). First, bismark_genome_preparation --bowtie2

was run to bisulfite convert and index the genome. The reference genome was GRCh37, downloaded from: http://ftp.ensembl.org/pub/grch37/current/fasta/homo_sapiens/dna/Homo_sapiens.GRCh37.dna.primary_assembly.fa.gz. Then mapping was performed with bismark --bowtie2 --bam in paired end mode. Reads were deduplicated with deduplicate_bismark --bam. Finally, methylation calls were extracted with bismark_methylation_extractor.

Quantification and Statistical Analysis

Data in the figure panels are presented as mean and ± standard deviation. Comparisons between two groups were evaluated using two-tailed, unpaired Student's t-tests using GraphPad Prism 9 software. Significant differences are noted at $p < 0.05$, and range of statistical significance is shown by an asterisk within the figure panels: ns = not significant, * = $p < 0.05$, ** = $p < 0.01$, *** = $p < 0.001$, **** = $p < 0.0001$. "N" denotes the number of biological replicates. If applicable to the experiment, technical replicates are shown next to biological replicates in brackets and separated by commas to denote number of technical replicates for each biological replicate. For example, for a panel quantifying markers expressed in imaged colonies, "N = 3 [3,1,2]" would denote 3 biological replicates with 3, 2, and 4 colonies (technical replicates) imaged per each biological replicate. For RNA sequencing, samples were collected from three experiments per experimental group (12 samples total: 3 TWT untreated (pluripotent), 3 TWT BMP4-treated, 3 TKD untreated (pluripotent), 3 TKD BMP4-treated). For whole genome bisulfite sequencing, samples were collected from three experiments per experimental group (6 samples total: 3 TWT untreated (pluripotent), 3 TKD untreated (pluripotent)).

Supplementary Material

Refer to Web version on PubMed Central for supplementary material.

ACKNOWLEDGEMENTS

This work was supported by the Core Center for iPS Cell Research, Research Center Network for Realization of Regenerative Medicine, AMED under grant number JP21bm0104001, the iPS Cell Research Fund, and the on-site laboratory initiative launched by Kyoto University. This work was also supported by funding from Mr. Hiroshi Mikitani, Mr. Marc and Mrs. Lynne Benioff, the L. K. Whittier Foundation, the Roddenberry Foundation, the Gladstone Institutes, the National Heart, Lung, and Blood Institute (NHLBI), the National Institutes of Health (NIH) (U01-HL100406, U01-HL098179, R01-HL130533, and R01-HL135358), the California Institute for Regenerative Medicine (CIRM) (LAI-C1408015), and Emergent Behaviors of Integrated Cellular Systems (EBICS) consortium (CBET0939511). Gladstone Institutes received support from National Center for Research Resources grant RR18928-01. Graphical illustrations and figure formatting were done by Tami Tolpa, Gladstone Institutes. Copy editing was done by Kathryn Claiborn, Gladstone Institutes.

REFERENCES

1. Tam PPL & Loebel DAF (2007). Gene function in mouse embryogenesis : get set for gastrulation. Nat. Rev. 8, 368–381.
2. Rossant J & Tam PPL (2009). Blastocyst lineage formation, early embryonic asymmetries and axis patterning in the mouse. Development 136, 701–713. [PubMed: 19201946]
3. Tam PPL & Behringer RR (1997). Mouse gastrulation : the formation of a mammalian body plan. Mech. Dev. 68, 3–25. [PubMed: 9431800]

4. Farquhar MG & Palade G (1963). Junctional complexes in various epithelia. J. Cell Biol. 17, 375–412. [PubMed: 13944428]
5. Claude P & Goodenough DA (1973). Fracture faces of zonulae occludentes from ‘tight’ and ‘leaky’ epithelia. J. Cell Biol. 58, 390–400. [PubMed: 4199658]
6. Zihni C, Mills C, Matter K & Balda MS (2016). Tight junctions : from simple barriers to multifunctional molecular gates. Nat. Rev. 17, 564–580.
7. Murphy SJ et al. (2004). Differential Trafficking of Transforming Growth Factor-Receptors and Ligand in Polarized Epithelial Cells. MBoC 15, 2853–2862. [PubMed: 15075369]
8. Yin X et al. (2017). Basolateral delivery of the type I transforming growth factor beta receptor is mediated by a dominant-acting cytoplasmic motif. MBoC 28, 2701–2711. [PubMed: 28768825]
9. Zhang Z, Zwick S, Loew E, Grimley JS & Ramanathan S (2019). Mouse embryo geometry drives formation of robust signaling gradients through receptor localization. Nat. Commun. 10, 1–14. [PubMed: 30602773]
10. Yamamoto H et al. (2013). The apical and basolateral secretion of Wnt11 and Wnt3a in polarized epithelial cells is regulated by different mechanisms. J. Cell Sci. 126, 2931–2943. [PubMed: 23613470]
11. Liu L et al. (2022). Nodal is a short-range morphogen with activity that spreads through a relay mechanism in human gastruloids. Nat. Commun. 13, 1–12. [PubMed: 34983933]
12. Phan-Everson T et al. (2021). Differential compartmentalization of BMP4/NOGGIN requires NOGGIN trans-epithelial transport. Dev. Cell 56, 1930–1944. [PubMed: 34051144]
13. Xiang L et al. (2020). A developmental landscape of 3D-cultured human pre-gastrulation embryos. Nature 577, 537–542. [PubMed: 31830756]
14. Turing AM (1952). The chemical basis of morphogenesis. Philos. Trans. R. Soc. 37–72 doi:10.1098/rstb.1952.0012.
15. Wolpert L (1969). Positional information and the spatial pattern of cellular differentiation. J. Theor. Biol. 25, 1–47. [PubMed: 4390734]
16. Green JBA & Sharpe J (2015). Positional information and reaction-diffusion: Two big ideas in developmental biology combine. Development 142, 1203–1211. [PubMed: 25804733]
17. Schier AF (2009). Nodal morphogens. Cold Spring Harb. Perspect. Biol. Biol 1, 1–20.
18. Müller P et al. (2012). Differential diffusivity of nodal and lefty underlies a reaction-diffusion patterning system. Science (80-.). 336, 721–724.
19. Etoc F et al. (2016). A Balance between Secreted Inhibitors and Edge Sensing Controls Gastruloid Self-Organization. Dev. Cell 39, 302–315. [PubMed: 27746044]
20. Tewary M et al. (2017). A stepwise model of Reaction-Diffusion and Positional-Information governs self-organized human peri-gastrulation-like patterning. Development dev.149658 doi:10.1242/dev.149658.
21. Warmflash A, Sorre B, Etoc F, Siggia ED & Brivanlou AH (2014). A method to recapitulate early embryonic spatial patterning in human embryonic stem cells. Nat. Methods 11, 847–854. [PubMed: 24973948]
22. Deglincerti A et al. (2016). Self-organization of human embryonic stem cells on micropatterns. Nat. Protoc. 11, 2223–2232. [PubMed: 27735934]
23. Ben-Haim N et al. (2006). The Nodal Precursor Acting via Activin Receptors Induces Mesoderm by Maintaining a Source of Its Convertases and BMP4. Dev. Cell 11, 313–323. [PubMed: 16950123]
24. Arnold SJ & Robertson EJ (2009). Making a commitment: Cell lineage allocation and axis patterning in the early mouse embryo. Nat. Rev. Mol. Cell Biol. 10, 91–103. [PubMed: 19129791]
25. Fanning AS & Anderson JM (2009). Zonula Occludens-1 and −2 Are Cytosolic Scaffolds That Regulate the Assembly of Cellular Junctions. Ann. N. Y. Acad. Sci. 1165, 113–120. [PubMed: 19538295]
26. Mcneil E, Capaldo CT & Macara IG (2006). Zonula Occludens-1 Function in the Assembly of Tight Junctions in Madin-Darby Canine Kidney Epithelial Cells. MBoC 17, 1922–1932. [PubMed: 16436508]

27. Libby ARG et al. (2018). Spatiotemporal mosaic patterning of pluripotent stem cells using CRISPR interference. Elife 7, 1–23.
28. Joy DA, Libby ARG & McDevitt TC (2021). Deep neural net tracking of human pluripotent stem cells reveals intrinsic behaviors directing morphogenesis. Stem Cell Reports 16, 1317–1330. [PubMed: 33979602]
29. Gunne-Braden A et al. (2020). GATA3 Mediates a Fast, Irreversible Commitment to BMP4-Driven Differentiation in Human Embryonic Stem Cells. Cell Stem Cell 26, 693–706. [PubMed: 32302522]
30. Nallet-Staub F et al. (2015). Cell Density Sensing Alters TGF-β Signaling in a Cell-Type-Specific Manner, Independent from Hippo Pathway Activation. Dev. Cell 32, 640–651. [PubMed: 25758862]
31. Smith Q et al. (2018). Cytoskeletal tension regulates mesodermal spatial organization and subsequent vascular fate. PNAS 115, 8167–8172. [PubMed: 30038020]
32. Manfrin A et al. (2019). Engineered signaling centers for the spatially controlled patterning of human pluripotent stem cells. Nat. Methods 16, 640–648. [PubMed: 31249412]
33. Kim Y et al. (2022). Cell position within human pluripotent stem cell colonies determines apical specialization via an actin cytoskeleton-based mechanism. Stem Cell Reports 17, 68–81. [PubMed: 34919810]
34. Stirling DR et al. (2021). CellProfiler 4: improvements in speed, utility and usability. BMC Bioinformatics 22, 1–11. [PubMed: 33388027]
35. Krtolica A et al. (2007). Disruption of Apical-Basal Polarity of Human Embryonic Stem Cells Enhances Hematoendothelial Differentiation. Stem Cells 25, 2215–2223. [PubMed: 17569786]
36. Mandegar MA et al. (2016). CRISPR Interference Efficiently Induces Specific and Reversible Gene Silencing in Human iPSCs. Cell Stem Cell 18, 541–553. [PubMed: 26971820]
37. Yadav S, Puri S & Linstedt AD (2009). A Primary Role for Golgi Positioning in Directed Secretion, Cell Polarity, and Wound Healing. MBoC 20, 1728–1736. [PubMed: 19158377]
38. Rodriguez-Boulan E & Macara IG (2014). Organization and execution of the epithelial polarity programme. Nat. Rev. Mol. Cell Biol. 15, 225–242. [PubMed: 24651541]
39. Fanning AS, Van Itallie CM & Anderson JM (2012). Zonula occludens-1 and −2 regulate apical cell structure and the zonula adherens cytoskeleton in polarized epithelia. Mol. Biol. Cell 23, 577–590. [PubMed: 22190737]
40. Ikenouchi J, Umeda K, Tsukita S, Furuse M & Tsukita S (2007). Requirement of ZO-1 for the formation of belt-like adherens junctions during epithelial cell polarization. J. Cell Biol. 176, 779–786. [PubMed: 17353356]
41. Rodgers LS, Tanner Beam M, Anderson JM & Fanning AS (2013). Epithelial barrier assembly requires coordinated activity of multiple domains of the tight junction protein ZO-1. J. Cell Sci. 126, 1565–1575. [PubMed: 23418357]
42. Umeda K et al. (2006). ZO-1 and ZO-2 Independently Determine Where Claudins Are Polymerized in Tight-Junction Strand Formation. Cell 126, 741–754. [PubMed: 16923393]
43. Van Itallie CM, Fanning AS, Bridges A & Anderson JM (2009). ZO-1 Stabilizes the Tight Junction Solute Barrier through Coupling to the Perijunctional Cytoskeleton. Mol. Biol. Cell 20, 3930–3940. [PubMed: 19605556]
44. Irie N et al. (2015). SOX17 is a critical specifier of human primordial germ cell fate. Cell 160, 253–268. [PubMed: 25543152]
45. Sasaki K et al. (2015). Robust In Vitro Induction of Human Germ Cell Fate from Pluripotent Stem Cells. Cell Stem Cell 17, 178–194. [PubMed: 26189426]
46. Muncie JM et al. (2020). Mechanical Tension Promotes Formation of Gastrulation-like Nodes and Patterns Mesoderm Specification in Human Embryonic Stem Cells. Dev. Cell 1–16 doi:10.1016/j.devcel.2020.10.015.
47. Sheng G (2015). Epiblast morphogenesis before gastrulation. Dev. Biol. 401, 17–24. [PubMed: 25446532]
48. Kinoshita M et al. (2021). Capture of Mouse and Human Stem Cells with Features of Formative Pluripotency Capture of Mouse and Human Stem Cells with Features of Formative Pluripotency. Cell Stem Cell 28, 1–19. [PubMed: 33417865]

49. Guo G et al. (2016). Naive Pluripotent Stem Cells Derived Directly from Isolated Cells of the Human Inner Cell Mass. Stem Cell Reports 6, 437–446. [PubMed: 26947977]
50. Takashima Y et al. (2014). Resetting transcription factor control circuitry toward ground-state pluripotency in human. Cell 158, 1254–1269. [PubMed: 25215486]
51. Theunissen TW et al. (2014). Systematic identification of culture conditions for induction and maintenance of naive human pluripotency. Cell Stem Cell 15, 471–487. [PubMed: 25090446]
52. Larripa K & Gallegos A (2017). A mathematical model of Noggin and BMP densities in adult neural stem cells. Lett. Biomath. 4, 1–22.
53. Jones CM & Smith JC (1998). Establishment of a BMP-4 Morphogen Gradient by Long-Range Inhibition. Dev. Biol. 194, 12–17. [PubMed: 9473328]
54. Farin HF et al. (2016). Visualization of a short-range Wnt gradient in the intestinal stem-cell niche. Nature 530, 340–354. [PubMed: 26863187]
55. Lawson KA et al. (1999). Bmp4 is required for the generation of primordial germ cells in the mouse embryo. Genes Dev. 13, 424–436. [PubMed: 10049358]
56. Arnold SJ, Maretto S, Islam A, Bikoff EK & Robertson EJ (2006). Dose-dependent Smad1, Smad5 and Smad8 signaling in the early mouse embryo. Dev. Biol. 296, 104–118. [PubMed: 16765933]
57. Libby ARG, Joy D, Elder NH, Bulger EA, Krakora MZ, Gaylord EA, Mendoza-Camacho F, Butts JC, and McDevitt TC (2021). Axial elongation of caudalized human organoids mimics aspects of neural tube development. Development 148, 1–16.
58. Köster J, and Rahmann S (2012). Snakemake-a scalable bioinformatics workflow engine. Bioinformatics 28, 2520–2522. [PubMed: 22908215]
59. Ewels P, Magnusson M, Lundin S, and K€aller M (2016). MultiQC: Summarize analysis results for multiple tools and samples in a single report. Bioinformatics 32, 3047–3048. [PubMed: 27312411]
60. Patro R, Duggal G, Love MI, Irizarry RA, and Kingsford C (2017). Salmon provides fast and bias-aware quantification of transcript expression. Nat. Methods 14, 417–419. [PubMed: 28263959]
61. Krueger F, and Andrews SR (2011). Bismark: A flexible aligner and methylation caller for Bisulfite-Seq applications. Bioinformatics 27, 1571–1572. [PubMed: 21493656]
62. Langmead B, and Salzberg SL (2012). Fast gapped-read alignment with Bowtie 2. Nat. Methods 9, 357–359. [PubMed: 22388286]
63. Schindelin J, et al. . (2012). Fiji: An open-source platform for biological-image analysis. Nat. Methods 9, 676–682. [PubMed: 22743772]
64. Hookway TA, Butts JC, Lee E, Tang H & McDevitt TC (2016). Aggregate formation and suspension culture of human pluripotent stem cells and differentiated progeny. Methods 101, 11–20. [PubMed: 26658353]
65. Ungrin MD, Joshi C, Nica A, Bauwens C & Zandstra PW (2008). Reproducible, ultra high-throughput formation of multicellular organization from single cell suspension-derived human embryonic stem cell aggregates. PLoS One 3, e1565. [PubMed: 18270562]

Highlights

- TJP1 establishes an epithelial barrier in hPSCs that is impermeable to BMP4.
- TJP1 KD results in ubiquitous and sustained pSMAD1/5 activity with BMP4 stimulation.
- TJP1 KD disrupts gastrulation patterning and leads to PGCLC differentiation in vitro.
- Bi-directional BMP4 stimulation mimics signaling/PGCLC specification seen with TJP1 KD.

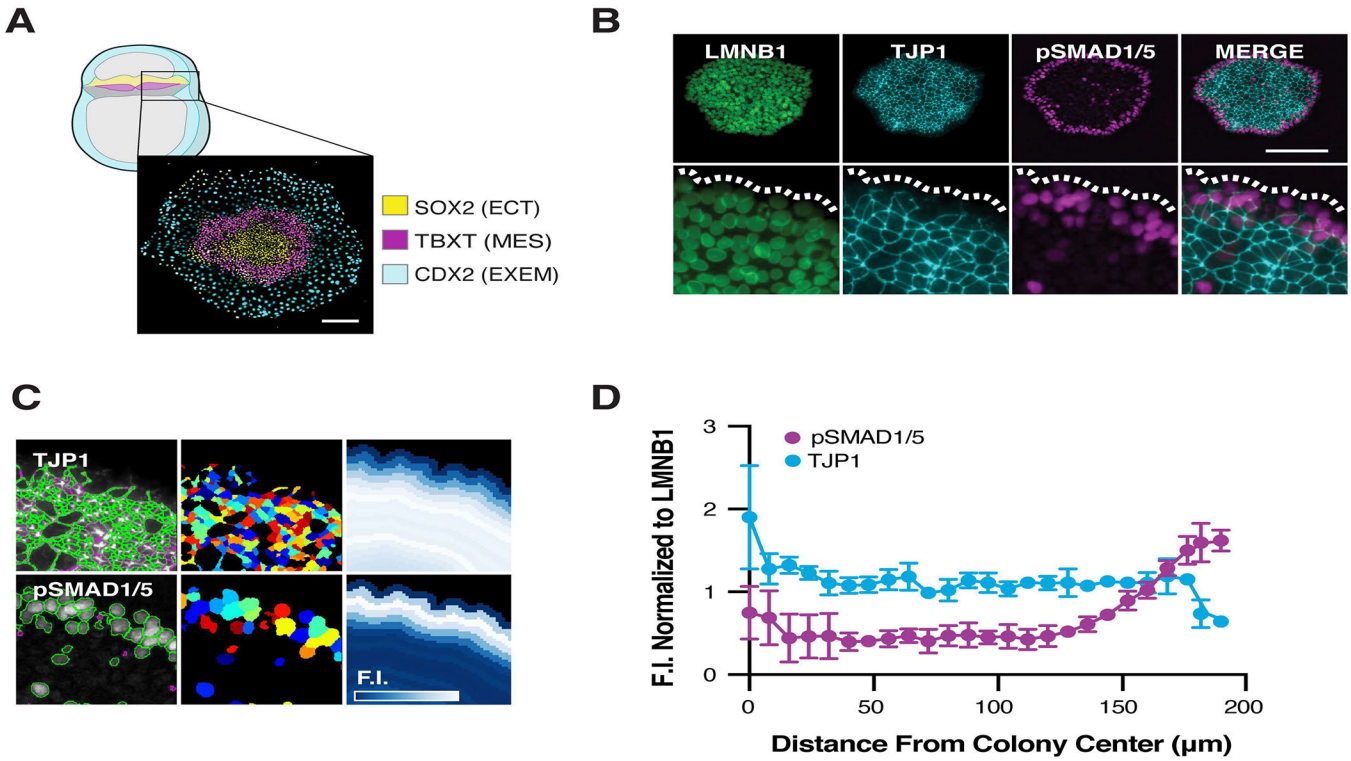

Figure 1: Unconfined hPSC colonies undergo radial gastrulation-like patterning and lose TJP1 on the colony edge.

1A: Unconfined circular colonies of hPSCs undergo radial patterning of gastrulation-associated markers after 48 hrs of BMP4 stimulation. ECT = ectoderm-like, MES = mesoderm-like, EXEM = extraembryonic-like. Scalebar depicts 200μm. 1B: IF image of the colony edge, showing regional loss of TJP1 which overlaps with pSMAD1/5 activity. Scalebar depicts 200μm. 1C: CellProfiler used to visualize and quantify expression of TJP1 and pSMAD1/5 within the colony. 1D. Quantification of loss of TJP1/gain of pSMAD1/5 on the colony edge, N = 3 [9,6,3].

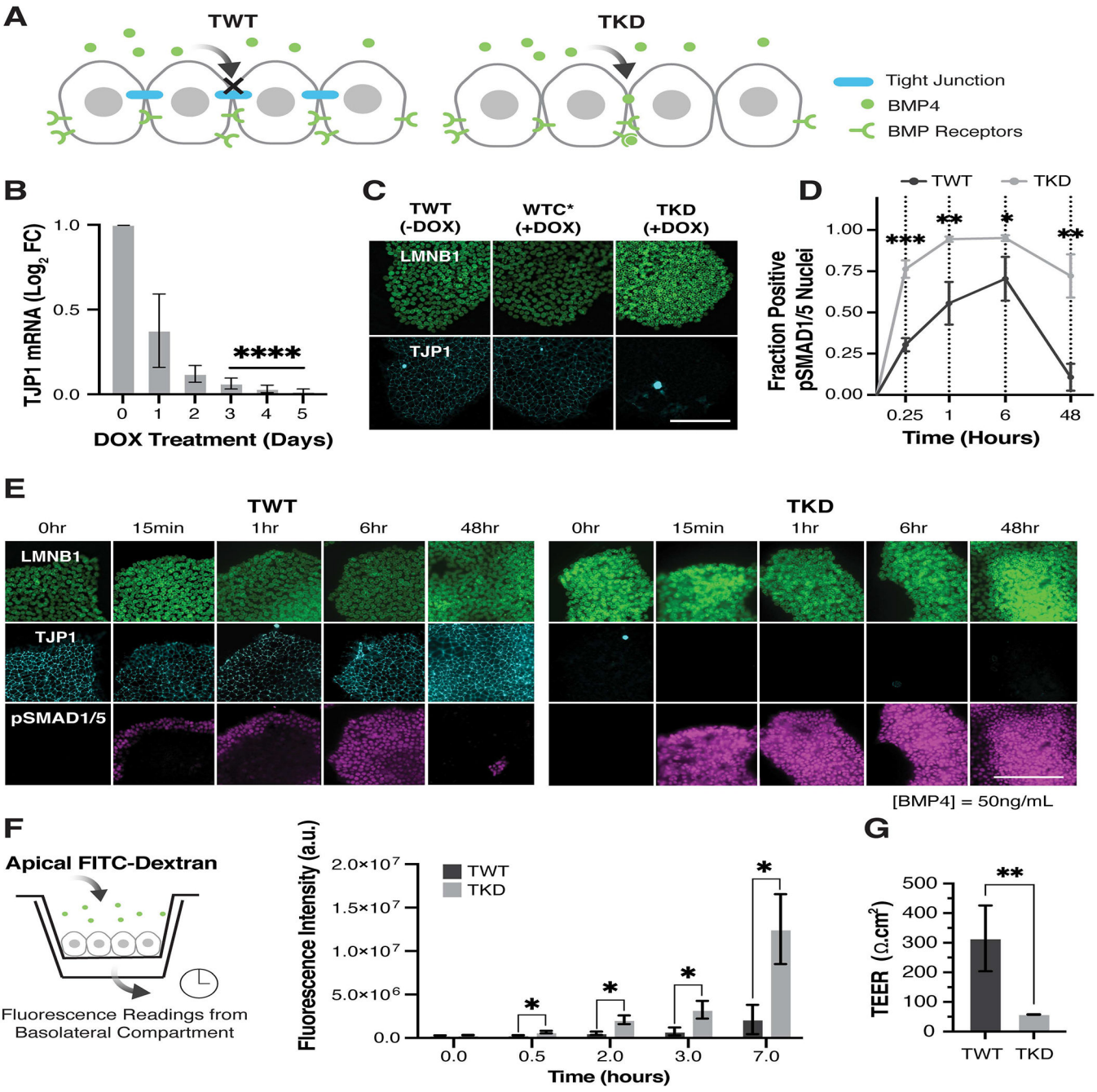

Figure 2: TKD causes ubiquitous and sustained phosphorylation of SMAD1/5 throughout the colony.

2A: Schematic depicting z-direction view of a cellular monolayer, with apical presentation of BMP4. BMP receptors are sequestered in the basolateral domain by tight junctions, rendering them inaccessible to BMP4 ligands. 2B: qPCR showing expression of TJP1 over time with DOX treatment and subsequent induction of dCas9 expression in the WTC TJP1 CRISPRi line, N = 5 [D0 (3,3,3,3,3); D1 (3,3,3,3,3); D2 (3,3,3,3,3); D3 (3,3,3,3,3); D4 (3,3,3,3,3); D5 (3,3,3,3,3)]. 2C: IF images showing TJP1 expression in the TWT/TKD lines (−/+ 5 days DOX) and the WTC CRISPRi parental line (no TJP1 guide expression, +5 days

DOX) shown in the central panel and denoted by "*". 2D: Quantification of pSMAD1+ cells over time using CellProfiler nuclear segmentation and co-localization. Plot indicates significant increases in pSMAD1/5 activation in TKD compared with TWT cells at all timepoints, N = 3 [TWT; 15min (6,5,4); 1hr (9,6,3); 6hr (8,6,4); 48hr (4,6,3)] and [TKD; 15min (7,7,4); 1hr (5,6,6); 6hr (6,6,4); 48hr (4,6,4)]. 2E: IF images showing sustained and ubiquitous phosphorylation of SMAD1/5 in TKD cells over the course of 48 hrs. Scalebar depicts 200μm. 2F: Schematic of FITC-dextran diffusion assay. TWT and TKD cells are cultured to confluence in a transwell plate, 40kDa FITC is applied to the apical side, and fluorescence measurements are taken from the basolateral compartment over time. Plot shows assay timepoints and indicates significant increases in diffusion of FITC-dextran in TKD compared with TWT monolayers at all timepoints. N = 3. 2G: TEER measurements in TWT and TKD monolayers, indicating increase in ion permeability in TKD compared with TWT monolayers. N = 3.

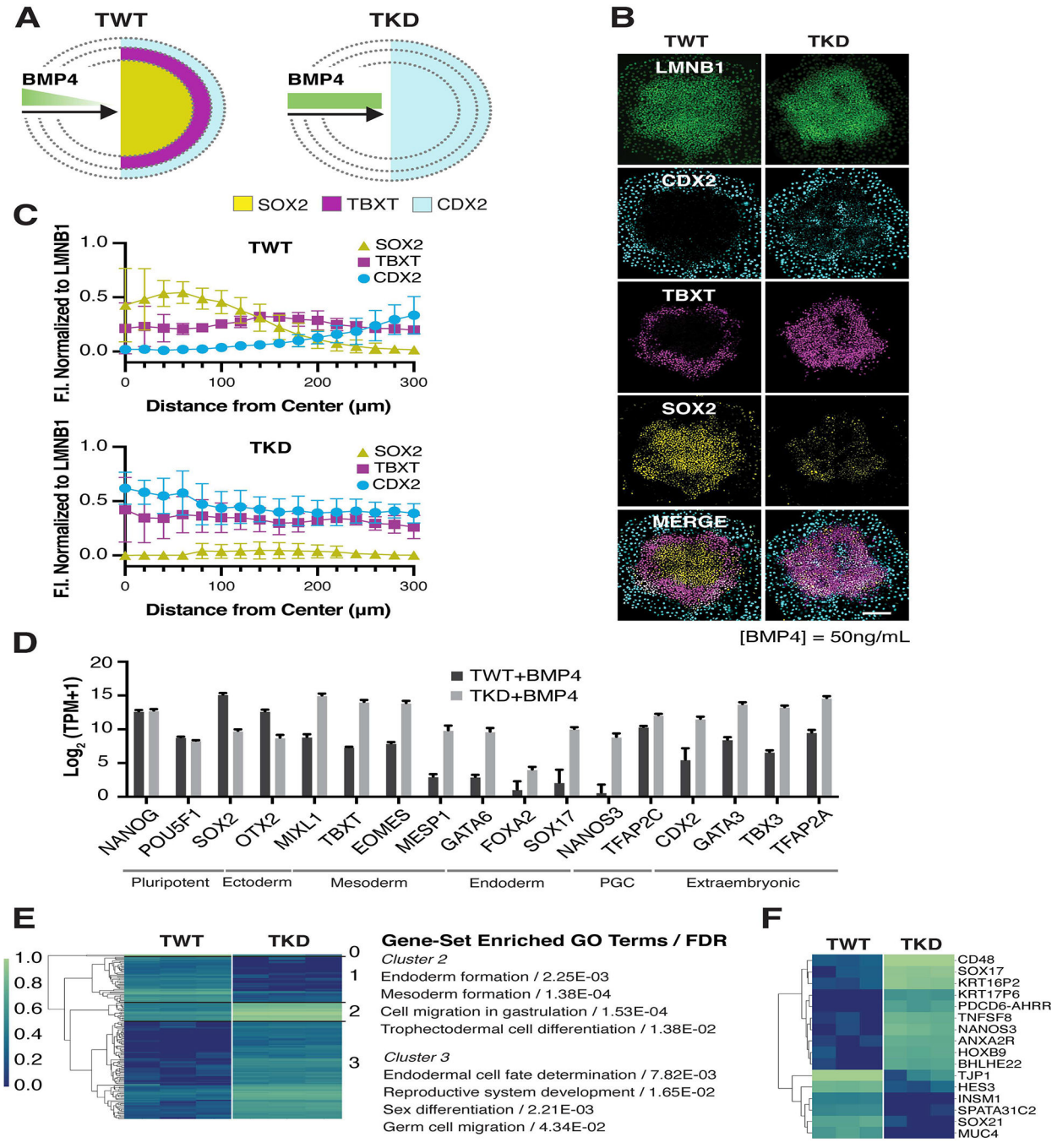

Figure 3: TKD causes changes in patterning and proportion of somatic germ lineages.

3A: Reaction diffusion and positional information paradigm and prediction in TWT (left) and TKD (right) unconfined colonies. Different transcription factor expression is shown in yellow (SOX2), magenta (TBXT), and cyan (CDX2). 3B: IF images of LMNB1, CDX2, TBXT, SOX2 in TWT and TKD colonies after 48 hrs of stimulation with BMP4. Scalebar depicts 200μm. 3C: Quantification of fluorescence intensity of CDX2, TBXT, and SOX2 at various radial positions from the colony edge indicating loss of patterning phenotype in TKD colonies, N = 3 [TWT (3,3,3); TKD (3,3,3)]. 3D: RNA sequencing data showing

expression of canonical gastrulation markers. TPM: transcripts per million, N = 3. 3E: Unbiased clustering and GO analysis of top 150 differentially expressed genes between TWT and TKD cells. 3F: Unbiased clustering of top 16 differentially expressed genes between TWT and TKD cells highlighting increases in PGCLC related genes. Colorbar scale in 3E, 3F represents standardized scale of Log_2(TPM+1) across each individual gene row.

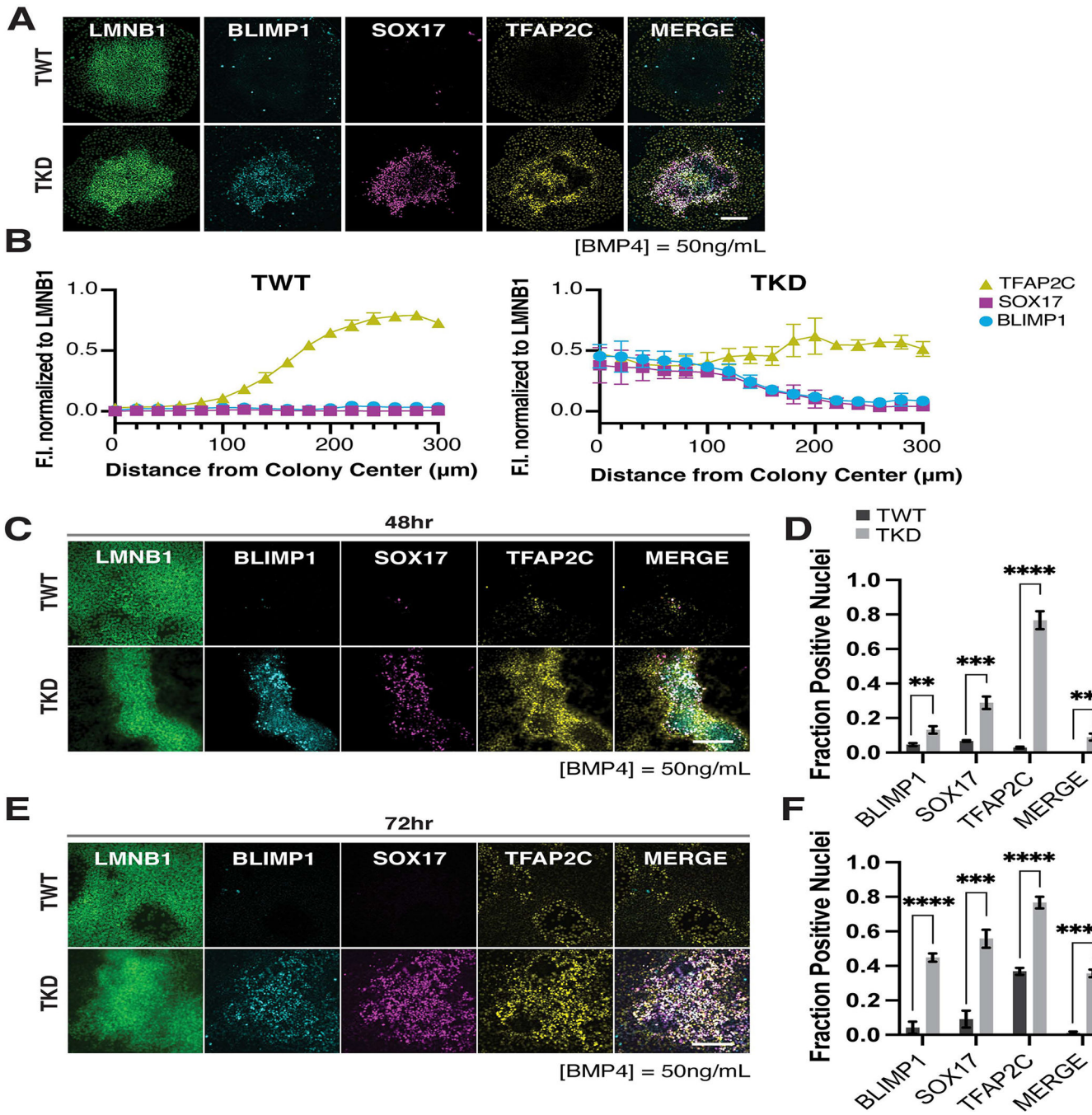

Figure 4: TKD cells have a bias for PGCLC differentiation.

4A: IF images of LMNB1, BLIMP1, SOX17, TFAP2C, in TWT and TKD unconfined colonies after 48 hrs of stimulation with BMP4. Scalebar depicts 200μm. 4B: Quantification of fluorescence intensity of BLIMP1, SOX17, TFAP2C at various radial positions from the colony edge, N = 3 [TWT (4,3,3); TKD (3,3,3)]. 4C, 4E: IF images of LMNB1, BLIMP1, SOX17, TFAP2C in TWT and TKD cells in standard monolayer culture after 48 hrs (C) and 72 (D) hrs of stimulation with BMP4. Scalebar depicts 200μm. 4D, 4F: Quantification of

PGC marker expression in TWT and TKD cells in standard monolayer culture after 48 hrs (C) and 72 (D) hrs of stimulation with BMP4, N = 3 [TWT (3,3,3); TKD (3,3,3)].

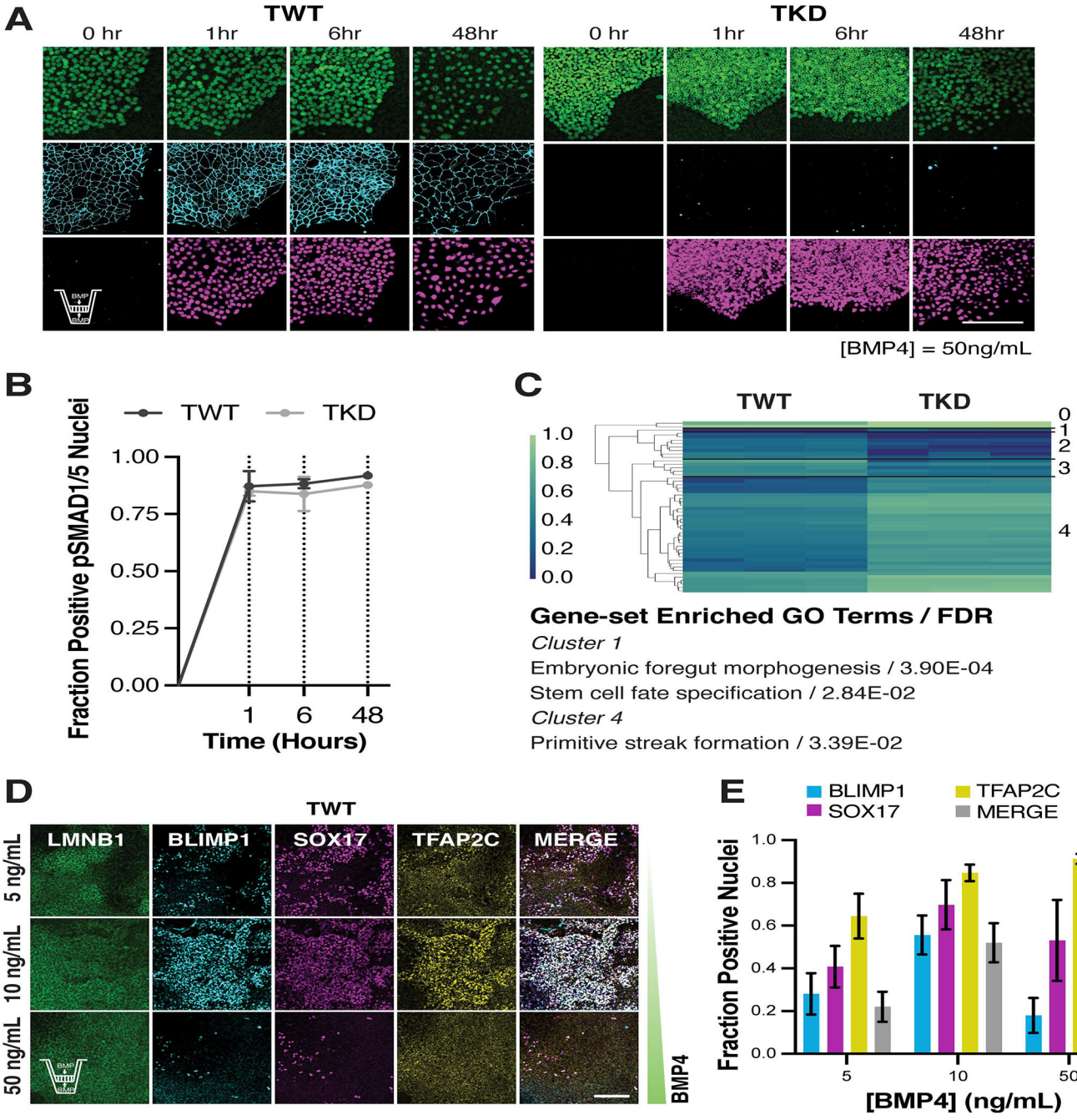

Figure 5: TJP1 KD-related PGCLC bias is a product of increased signaling.

5A: IF images of pSMAD1/5 after bi-directional BMP4 stimulation of TWT and TKD unconfined colonies grown on transwell membranes from timepoints between 0–48 hrs. Scalebar depicts 200μm. 5B: Quantification of pSMAD1/5 positive cells in TWT and TKD unconfined colonies grown on transwells and stimulated bi-directionally with BMP4 for 0–48 hrs, N = 3 [TWT; 1hr (3,3,3); 6hr (3,3,3); 48hr (3,3,3)] and [TKD; 1hr (3,3,3); 6hr (4,3,4); 48hr (3,3,4)]. 5C: Unbiased clustering and GO analysis of all differentially expressed genes between TWT and TKD cells. Colorbar scale represents standardized scale of Log_2(TPM+1) across each individual gene row. 5D: IF images of LMNB1,

BLIMP1, SOX17, TFAP2C in TWT cells grown as a monolayer at a seeding density of 1,000cells/mm^2 on transwell membranes after 48 hrs of bi-directional (apical and basolateral) stimulation with BMP4 (concentrations between 5–50ng/mL). Scalebar depicts 200μm. 5E: Quantification of fraction positive nuclei for each marker (BLIMP1, SOX17, TRAP2C, and triple positive MERGE), N = 3 [5 ng/mL (3,3,4); 10 ng/mL (4,3,3); 50ng/mL (3,3,3)].

Key Resources Table

REAGENT or RESOURCE	SOURCE	IDENTIFIER
Antibodies		
Mouse monoclonal anti-ZO1	Thermo Fisher Scientific	Cat# 33–9100, RRID:AB_2533147
Rabbit monoclonal anti-phospho SMAD1/5	Cell Signaling Technology	Cat# 9516, RRID:AB_491015
Mouse monoclonal anti-CDX2	Abcam	Cat# ab157524, RRID:AB_2721036
Goat polyclonal anti-Brachyury/TBXT	R & D Systems	AF2085, RRID:AB_2200235
Rabbit monoclonal anti-SOX2	Cell Signaling Technology	Cat# 3579, RRID:AB_2195767
Rabbit monoclonal anti-Golgin97	Cell Signaling Technology	Cat# 13192, RRID:AB_2798144
Rabbit polyclonal anti-BMPR1A	Thermo Fisher Scientific	Cat# 38–6000, RRID:AB_2533377
Mouse monoclonal anti-Ezrin	BD Biosciences	Cat# 610603, RRID:AB_397940
Mouse monoclonal anti-PKC	Santa Cruz Biotechnology	Cat# sc-17781, RRID:AB_628148
Mouse monoclonal anti-PARD6B	Santa Cruz Biotechnology	Cat# sc-166405, RRID:AB_2267890
Mouse monoclonal anti-PRDM1/BLIMP1	R & D Systems	Cat# MAB36081, RRID:AB_10718104
Goat polyclonal anti-SOX17	R & D Systems	Cat# AF1924, RRID:AB_355060
Rabbit monoclonal anti-AP2 gamma/TFAP2C	Abcam	Cat# ab218107, RRID:AB_2891087
Donkey polyclonal anti-mouse IgG H&L (Alexa Fluor 555)	Abcam	Cat#: ab150106, RRID:AB_2857373
Donkey polyclonal anti-rabbit IgG H&L (Alexa Fluor 647)	Abcam	Cat#: ab150075, RRID:AB_2752244
Donkey polyclonal anti-goat IgG H&L (Alexa Fluor 405)	Abcam	Cat#: ab175664, RRID:AB_2313502
Chemicals, peptides, and recombinant proteins		
Recombinant human BMP-4	R & D Systems	Cat#: 314-BP
Y-276932 (ROCK inhibitor)	Selleckchem	Cat#: S6390
Growth factor reduced (GFR) Matrigel	Corning	Cat#: 356231
mTESR1	Stem Cell Technologies	Cat#: 85850
G418 (Geneticin)	Thermo Fisher Scientific	Cat#: 10131035
Blasticidin	Thermo Fisher Scientific	Cat#: A1113903
Fluorescein isothiocyanate (FITC) –dextran (40 kDa molecular weight)	Sigma Aldrich	CAS#: 60842–46-8
Paraformaldehyde	VWR	CAS#: 50–00-0
Triton X-100	Sigma Aldrich	CAS#: 9036–19-5
Critical commercial assays		
RNeasy Mini Kit	Qiagen	Cat#: 74104

REAGENT or RESOURCE	SOURCE	IDENTIFIER
DNeasy Blood & Tissue Kit	Qiagen	Cat#: 69504
Human Stem Cell Nucleofector Kit 1	Lonza	Cat#: VPH-5012
MycoAlert Mycoplasma Detection Kit	Lonza	Cat#: LT07–710
Human NOGGIN ELISA Kit	Abcam	Cat#: ab283879
Deposited data		
RNA Sequencing Data	This paper	GEO: GSE213911
Bisulfite Sequencing Data	This paper	SRA: PRJNA880895
Human reference genome, GRCh38 (used for RNA Sequencing analysis)	Genome Reference Consortium	http://ftp.ensembl.org/pub/release-104/fasta/homo_sapiens/cdna/Homo_sapiens.GRCh38.cdna.all.fa.gz
Human reference genome, GRCh37 (used for Bisulfite Sequencing analysis)	Genome Reference Consortium	http://ftp.ensembl.org/pub/grch37/current/fasta/homo_sapiens/dna/Homo_sapiens.GRCh37.dna.primary_assembly.fa.gz
RNA Sequencing analysis pipeline	This paper	https://github.com/amaslan/rna-seq-analysis-pipeline DOI: 10.5281/zenodo.7556156
Bisulfite Sequencing analysis pipeline	This paper	https://github.com/amaslan/bisulfite-pipeline DOI: 10.5281/zenodo.7556158
Image analysis pipeline	This paper	https://github.com/ivanavasic/image_analysis DOI: 10.5281/zenodo.7562870
Experimental models: Cell lines		
Human: WTC-mEGFP-LMNB1-cl210 iPS cell line	Allen Institute	Cat#: AICS-0013, RRID: CVCL_IR32
Human; WTC-mEGFP-LMNB1-CRISPRi iPS cell line	Libby et al., 2021[57]	N/A
Human: TJP1 KD WTC-mEGFP-LMNB1 cell line (in text: TWT and TKD)	This paper	N/A
Human: WTB Gen1B CRISPRi iPS cell line	Gladstone Stem Cell Core, Mandegar et al., 2016[36]	RRID: CVCL_VM35
Human: TJP1 KD WTB Gen1B CRISPRi iPS cell line (in text WTB TWT and TKD)	This paper	N/A
Oligonucleotides		
TJP1/ZO1 guide sequence: CCGGTTCCCGGGAAGTTACG	Integrated DNA Technologies	N/A
Recombinant DNA		
pgRNA-CKB plasmid	Addgene	RRID:Addgene_73501
pgRNA-CKB (with TJP1/ZO1 guide) plasmid	This paper	N/A
pAAVS1-NDi-CRISPRi (Gen2) plasmid	Addgene	RRID:Addgene_73498
Software and algorithms		
Python (v3.6.10)	Python	https://www.python.org/
Snakemake (v3.13.3)	Koster et al., 2012[58]	https://snakemake.readthedocs.io/en/v3.13.3/
FastQC (v0.11.9)	Babraham Institute	https://github.com/s-andrews/FastQC and https://www.bioinformatics.babraham.ac.uk/projects/fastqc/
MultiQC (v1.9)	Ewels et al., 2016[59]	https://github.com/ewels/MultiQC
Salmon (v0.14.2)	Patro et al., 2017[60]	https://github.com/COMBINE-lab/salmon
Bismark (v0.22.3)	Krueger et al., 2011[61]	https://bioweb.pasteur.fr/packages/pack@bismark@v0.22.3

REAGENT or RESOURCE	SOURCE	IDENTIFIER
Bowtie2 (v2.3.4.1)	Langmead and Salzberg, 2012[62]	http://bowtie-bio.sourceforge.net/bowtie2/index.shtmL
CellProfiler	Stirling et al., 2021[34]	https://cellprofiler.org
FIJI (ImageJ 1.52a or later, using Java 1.8.0_172 or later)	Schindelin et al., 2012[63]	https://imagej.net/Fiji
Prism 9	GraphPad	https://www.graphpad.com/scientific-software/prism/
Other		
Costar Transwell plates	Corning	Cat#: 07–200-147